Nano Energy 63 (2019) 103845

Contents lists available at ScienceDirect

Nano Energy

journal homepage: www.elsevier.com/locate/nanoen

Full paper

High-performance silicon-carbon anode material via aerosol spray drying and magnesiothermic reduction

Zheng Yan[a], Juchen Guo[a,b,*]

[a] Department of Chemical and Environmental Engineering, University of California – Riverside, Riverside, 92521, United States
[b] Materials Science and Engineering Program, University of California – Riverside, Riverside, 92521, United States

ARTICLE INFO

Keywords:
Aerosol spray drying
Li-ion batteries
Magnesiothermic reduction
Silicon-carbon composite

ABSTRACT

We report a high-performance silicon-carbon (Si-C) composite anode material for lithium-ion (Li-ion) batteries via a scalable production route. Porous silica particles as the precursor of Si is obtained from aerosol spray drying of the commercial silica suspension in water. The silica particles are reduced to porous Si via magnesiothermic reduction followed by carbon coating from chemical vapor deposition (CVD). The kinetics of magnesiothermic reduction of silica is systematically studied thus the conversion and the microstructural properties of obtained porous Si can be precisely optimized. The Si-C composite demonstrates excellent specific capacity of 1835 mAh g^{-1} and outstanding cycle stability. When used as an additive to the graphite anode, the thick electrodes with total areal loading of 4.0 mg cm^{-2} containing 20 wt% Si-C and 70 wt% graphite achieve remarkable performance: 850 mAh g^{-1} overall specific capacity and 3.4 mAh cm^{-2} areal capacity as well as 92% capacity retention after 200 cycles. Full cells composed of commercial lithium iron phosphate cathode and the Si-C-graphite anode under lean electrolyte condition also demonstrate excellent performance.

1. Introduction

Silicon (Si) is a high-capacity anode material that can replace or complement the graphite anode in the next generation lithium-ion (Li-ion) batteries [1–15]. Tremendous efforts from both academic and industrial sectors are devoted to develop Si-based anode materials [10,16–19]. However, successful commercialization of Si-anodes is still scarce. The technical challenges are mostly originated from two fundamental properties of Si as the Li storage material: inevitable volume change during lithiation-delithiation and inferior electronic conductivity comparing to graphite. The former results to continuous degradation of the electronic connection in the electrodes and continuous rapture of the solid electrolyte interphase (SEI); [3,20–25] the latter seriously limits the areal loading of the Si-based materials in the electrode, thus difficult to achieve practical high-capacity [9,12,26–28]. In addition to addressing the technical challenges, establishing a production process is equally important to the commercialization of Si-based anode materials. Such a process not only must be scalable with economic feasibility but also technologically robust to achieve optimal properties of the Si-based anode materials.

Among the numerous production methods reported to date, magnesiothermic reduction reaction (MRR) remains a viable candidate for Si material production process. Since Bao and co-workers reported Si synthesis via thermal reduction of silicon oxide by magnesium (Mg), [29–31] many Si-based anode materials synthesized from MRR has been reported [4,32–38]. However, certain challenges still remain: Due to the exothermic nature of MRR, it is difficult to control the microstructure of the obtained Si due to the fusion of Si [39]. Generation of byproducts including magnesium silicate (Mg_2SiO_4) and magnesium silicide (Mg_2Si) is another severe challenge of MRR [40,41]. These byproducts are induced due to discrepant atoms mobilities in Si-Mg-O system and the chemical stability of the interface between MgO, SiO_2 and Si [42]. Finally, the kinetics of MRR is not well understood therefore it has been difficult to optimize the MRR process. In this work, we started with preparing the precursor from the commercial silica suspension in water (LUDOX HS-40) via a simple spray drying process, followed by a thorough investigation of the kinetics of the magnesiothermic reduction of the silica particles. From the kinetic study, porous Si particles with optimal conversion, microstructure, and electrochemical properties were produced. After carbon coating via chemical vapor deposition (CVD), the final Si-C composite product demonstrated superior performance as the Li-ion anode material under commercially relevant testing conditions.

* Corresponding author. Department of Chemical and Environmental Engineering, University of California – Riverside, Riverside, 92521, United States.
E-mail address: jguo@engr.ucr.edu (J. Guo).

https://doi.org/10.1016/j.nanoen.2019.06.041
Received 26 April 2019; Received in revised form 18 June 2019; Accepted 18 June 2019
Available online 22 June 2019

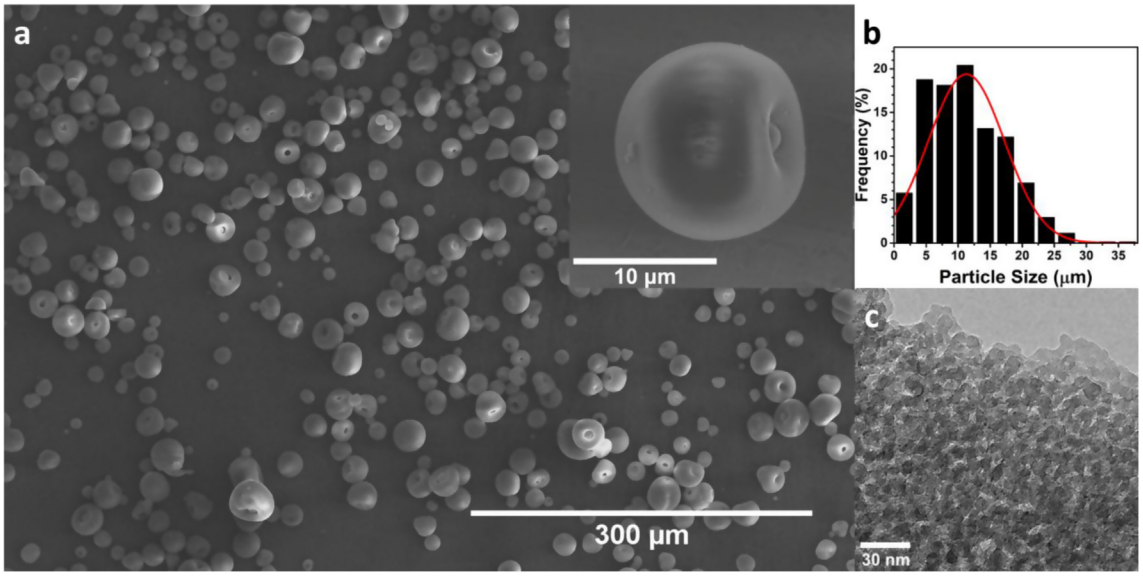

Fig. 1. (a) SEM image of the silica particles obtained from aerosol spray drying (inset is a particle under high magnification); (b) silica particle size distribution; and (c) TEM image showing the primary silica particles.

2. Experimental section

Si-C Production: Commercial silica water suspension (LUDOX HS-40) was diluted with deionized water from 40 wt% solid content to 20 wt%. The obtained suspension was spray-dried with an industrial aerosol spray dryer at 150 °C. The obtained spray-dried silica powder was thoroughly mixed with the magnesium (Mg) powder (300 mesh) with a molar ratio of $Mg:SiO_2 = 2.2:1$ under argon environment. In the MRR experiments with heat scavenger, sodium chloride (NaCl) with mass ratio Mg:NaCl = 1:1 was added in the mixture. In a typical MRR, 2.7 g of the mixture was sealed in a stainless-steel reactor (5 mL) under argon. The reactor was heated in a tube furnace at 1 °C min^{-1} from room temperature to the isothermal step temperature (580 °C, 680 °C, or 780 °C). The isothermal step was 1 h, 3 h, 6 h, 9 h or 12 h followed by natural cooling to room temperature. The obtained material was rinsed with 45 mL of 2 M HCl solution (H_2O: Ethanol = 1:1 by volume) for 12 h to remove MgO and unreacted Mg, then 1 mL HF (49 wt%) was added into the solution to remove unreacted silica. The resultant Si materials were washed with water and collected via filtration. Final products were dried in vacuum oven for 12 h. Carbon coating was performed via CVD in a rotating tube furnace. In a typically CVD process, 1.0 g of Si was loaded in the tube reactor. After purging with argon (100 sccm) for 60 min, the reactor was heated with a ramp rate of 10 °C min^{-1} to 700 °C. After reaching the temperature, acetylene (C_2H_2) and argon gas mixture was introduced with flow rate $C_2H_2/Ar = 10/20$ sccm while rotating the tube reactor. After certain time (depending on the targeted ratio of carbon coating), the acetylene feed was cut off and the reactor was naturally cooled down to room temperature.

Material Characterizations: The crystalline compounds after MRR and after acid rinsing were analyzed by X-ray diffraction (XRD, PANalytical EMPYREAN) with a CuKα source. The morphology and microstructure of the Si and Si-C were analyzed by transmission electron microscopy (TEM, Tecnai 12) and scanning electron microscope (SEM, Nova NanoSEM 450). The surface area was measured from the N_2 adsorption and desorption isotherms with the Brunauer-Emmett-Teller (BET) method with an ASAP 2020 instrument. TGA was performed by a TA Instrument analyzer (Q 500) at ramp rate of 10 °C min^{-1} from room temperature to 600 °C in dry air with a 60 min isothermal step at 600 °C.

Electrochemical Analyses: Electrochemical analyses were performed with two-electrode 2032-type coin cells. In the half-cells to test the pure Si materials from MRR and the Si-C composites after carbon coating, the working electrode was composed of 80 wt% of Si (or Si-C), 10 wt% of sodium carboxymethyl cellulose (CMC), and 10 wt% of acetylene black. The typical areal loading of pure Si or Si-C was 1 mg cm^{-2}. The Si-C-graphite electrode was composed of 90 wt% Si-C and graphite, 4 wt% of CMC, 1 wt% of styrene-butadiene, and 5 wt% of acetylene black. The typical areal loading of Si-C and graphite was 4.1 mg cm^{-2}. The electrolyte was composed of Lithium hexafluorophosphate ($LiPF_6$) solution (1 M) in a mixture of ethylene carbonate (EC), diethyl carbonate (DEC) and fluoroethylene carbonate (FEC) (volume ratio EC: DEC: FEC = 45:45:10). Commercial lithium foil (750 μm thickness) was used as the counter electrode. Galvanostatic cycling was performed between 0.01 and 1.2 V vs Li/Li^+ in half cells. The current density for Si and Si-C electrode was 100 mA g^{-1}. The current density for Si-C-graphite electrodes was 0.1 mA cm^{-2} at first cycle and then 0.5 mA cm^{-2} or 1.0 mA cm^{-2} for the subsequent cycles. In the full cell tests, the $LiFePO_4$ cathode was composed of 90 wt% of $LiFePO_4$ powder, 5 wt% polyvinylidene fluoride and 5 wt% of acetylene black with typical areal loading of 20 mg cm^{-2}. In either half-cell or full cell tests, the amount of electrolyte was controlled at 14 μL per cell. The full cells were cycled between 2.0 V and 3.6 V with 0.5 mA cm^{-2} or 1.0 mA cm^{-2} current density. The full cells were charged with constant-current-constant-voltage method. The constant voltage was 3.6 with a cut-off current of 0.05 mA cm^{-2}.

3. Results and discussion

Silica particles were first produced from an aerosol spray drying process illustrated in Figure S1 (Supporting Information). In brief, commercial silica water suspension (LUDOX HS-40 with 40 wt% silica content) was diluted with water and atomized with a two-fluid atomizer nozzle. The generated aerosol was carried into a stainless-steel dryer at 150 °C by nitrogen gas to obtain the dried silica particles, of which the scanning electron microscopic (SEM) and transmission electron microscopic (TEM) images are displayed in Fig. 1. The average size of the silica particle is 11 μm as indicated by the particle size distribution in Fig. 1b. Each particle is composed of many 10-nm primary silica particles (Fig. 1C), which is consistent with the particle size of silica in LUDOX HS-40. The BET specific surface area of the silica particles is 178 $m^2 g^{-1}$ measured from nitrogen adsorption-desorption isotherms (Figure S2 in Supporting Information).

The obtained silica particles were subsequently reduced to Si via

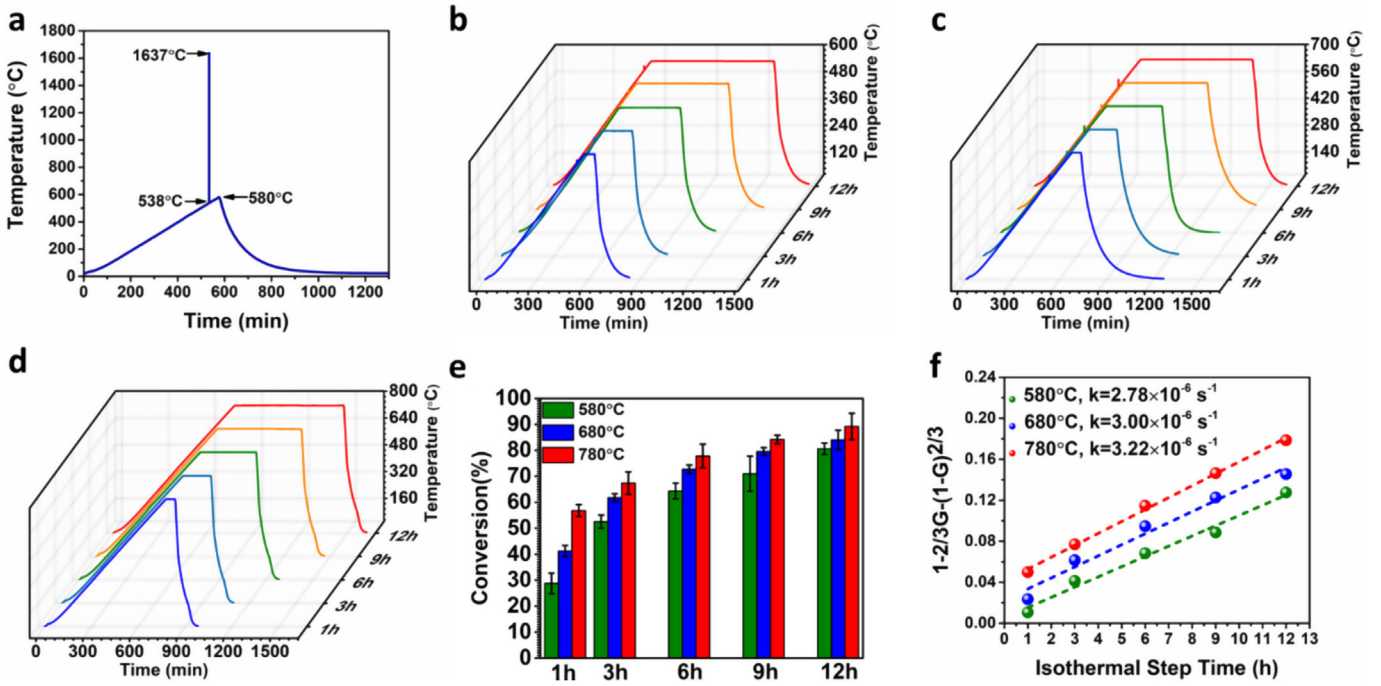

Fig. 2. (a) Temperature profile of the MRR without NaCl in the reactant mixture of silica and Mg powder; Temperature profiles of MRR with NaCl as the heat scavenger (weigh ratio Mg:NaCl = 1:1) for isothermal step at (b) 580 °C, (c) 680 °C, and (d) 780 °C with different isothermal step duration; (e) The silica-to-Si conversion under different reaction temperature and duration; (f) Ginstling-Brounshtein model fitting with the conversion data to obtain the reaction rate constant at different reaction temperature.

MRR process. The mixture of silica particles and Mg powder (300 mesh) was sealed in a home-made stainless-steel reactor under argon and the reactor was heated to 580 °C with a rate of 1 °C min^{-1}. To measure the onset temperature of the MRR, a high-temperature thermocouple was inserted in the home-made stainless-steel reaction (the image of the reactor with the thermocouple is shown in Figure S3 in Supporting Information). As shown in Fig. 2a, a temperature spike occurred at 538 °C and the highest temperature recorded by the thermocouple is 1673 °C. Although the temperature spike only lasted no more than 5 seconds (the heat was dissipated through the stainless-steel body of the reactor), it significantly undermined the quality of the product by forming a considerable amount of Mg_2SiO_4 (Figure S4 in Supporting Information). The formation of Mg_2SiO_4 is previously reported due to the high-temperature promoted partial reduction of silica by Mg to form $MgSiO_3$, which is further reacted to Mg to form Mg_2SiO_4 [42,43]. It is also observed that Mg_2Si can also be generated from the MRR with prolonged reaction time (Figure S4 in Supporting Information). To alleviate the impact of this exothermic process, sodium chloride (NaCl) was added into the reactant mixture as the heat scavenger [44,45]. With the addition of NaCl (mass ratio Mg:NaCl = 1:1), MRR under different reaction (isothermal step) temperatures (580 °C, 680 °C and 780 °C) and reaction durations (1 h, 3 h, 6 h, 9 h, and 12 h) were performed. Fig. 2b–d show the temperature profiles in the reactor as the function of time. It is clear that NaCl effectively absorbed the heat released by MRR thus no temperature spike was observed. The powder X-ray diffraction (XRD) pattern in Fig. 3a indicates that the products from MRR at 580 °C contain magnesium oxide (MgO), Si and NaCl without indication of Mg_2Si or Mg_2SiO_4 byproducts. After rinsing the product with hydrochloric acid and hydrofluoric acid to remove NaCl, MgO and unreacted silica, the XRD pattern of the final product (Fig. 3b) indicates crystal Si. The silica-to-Si conversion at different reaction temperature and duration was also obtained as shown in Fig. 2e. As expected, the conversion (from triplicate experiments) increases with increasing reaction temperature and reaction duration. The conversion results fit excellently to the Ginstling-Brounshtein model, which is a kinetics model for solid-state reaction under high yield condition: [46,47].

$$\boldsymbol{kt} = 1 - \frac{2}{3}\boldsymbol{G} - (1 - \boldsymbol{G})^{\frac{2}{3}} \quad (1)$$

where $\boldsymbol{k}$ is the MRR rate constant, $\boldsymbol{G}$ is the conversion, and $\boldsymbol{t}$ is the isothermal step time. As shown in Fig. 2f, the MRR rate constant obtained from the fitting at 580 °C, 680 °C and 780 °C is 2.78 × 10^{-6} s^{-1}, 3.0 × 10^{-6} s^{-1} and 3.22 × 10^{-6} s^{-1}, respectively. With the rate constants, the effective activation energy of the MRR (with NaCl as heat scavenger) in the temperature range 580–780 °C is calculated as 5.5 kJ mol^{-1}. The low activation energy indicates the MRR is a mass transfer limited process. Furthermore, the silica-to-Si conversion can be predicated as a function of time with the reaction rate constants (Figure S5 in Supporting Information).

The kinetics of the MRR (i.e., different reaction temperature and duration) not only affected the conversion, but also the microstructure of the obtained Si. The full width at half maximum of the XRD peaks of the Si produced at 580 °C (Fig. 3b) indicates the size of the Si crystal grains grows with increasing reaction duration. This observation is confirmed by the TEM images of the Si displayed in Fig. 4, which clearly illustrate that the porosity of Si from MRR decreases monotonically with the increasing reaction duration. The specific BET surface area of these Si materials in Fig. 4f further confirms the finding: All Si from MRR at 580 °C have lower specific surface area than that of the precursor silica particles (178 $m^2 g^{-1}$). Their specific surface area decreases from 113.8 $m^2 g^{-1}$ (1 h reaction) to 22.6 $m^2 g^{-1}$ (12 h reaction) monotonically with increasing reaction duration.

Si produced from MRR at 580 °C were examined as the anode in half-cells with Li foil as the counter electrode. The electrode is composed of 80 wt% of Si, 10 wt% of sodium carboxymethyl cellulose (CMC) as binder, and 10 wt% of acetylene black with a typical areal loading of 1 mg of Si per cm^2. Fig. 5a shows the cycle stability and Coulombic efficiency (CE) (from triplicate experiments) under lithiation-delithiation rate of 100 mA g^{-1}. The Si produced from 6 h reaction has the highest capacity retention: It delivered 3562 mAh g^{-1} in the first lithiation and retaining 1344 mAh g^{-1} capacity after 100 cycles. It is worth noting that there is a significant irreversible capacity between

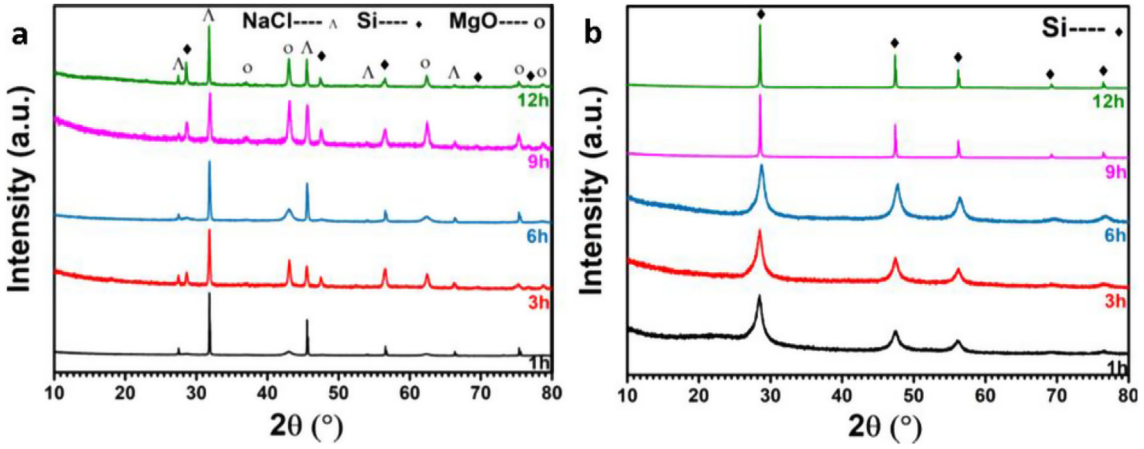

Fig. 3. XRD patterns of (a) products from MRR at 580 °C with NaCl (Mg:NaCl = 1:1) for 1 h, 3 h, 6 h, 9 h and 12 h and (b) products after rinsing with hydrochloric acid and hydrofluoric acid.

the 1st and 2nd lithiation in all electrodes, which leads to the low initial Coulombic efficiency (ICE). To better understand the origin of the low ICE, we calculated ICEs from two different methods as illustrated in Figure S6 in Supporting Information. The first ICE (the conventional definition) is the ratio of delithiation capacity to the total lithiation capacity; the second one is the ratio between the lithiation capacity attributed to Si and the total lithiation capacity. The capacity from lithiation of Si is defined as the capacity below 0.13 V versus Li^+/Li based on the previous study by Li and Dahn on lithiation-induced phase change of Si [48]. This definition is also consistent with the general observation in the literature. As displayed in Fig. 5b, the ICEs based on the second method (red columns) are significantly higher the conventional ICEs (blue columns): which means the low conventional ICE is clearly attributed to the irreversible capacity lost from delithiation of Si. The irreversibility can be attributed to the insulating nature of the Si and the worsened electronic contact induced by volume expansion.

Carbon coating has been proven an effective strategy to alleviate the challenges revealed above [49–57]. However, certain criteria of carbon coating have to be satisfied: The carbon coating should not promote undesired side reactions. Thus, carbon with intrinsic porous structure and rich functional groups containing heteroatoms (typically oxygen and nitrogen) is poor choice. Furthermore, the carbon coating needs to be conformal to not increase the accessible surface area and minimize the required amount of carbon. Based on these criteria, we selected chemical vapor deposition (CVD) as the carbon coating method in this study [58–62]. Based on an overall consideration for optimal conversion, reaction temperature and duration, and cycle stability, Si from MRR at 580 °C for 6 h was selected for carbon coating. Si-C composites with different ratio of carbon coating of 9 wt%, 12 wt% and 16 wt% (measured by thermogravimetric analysis in Figure S7 in Supporting

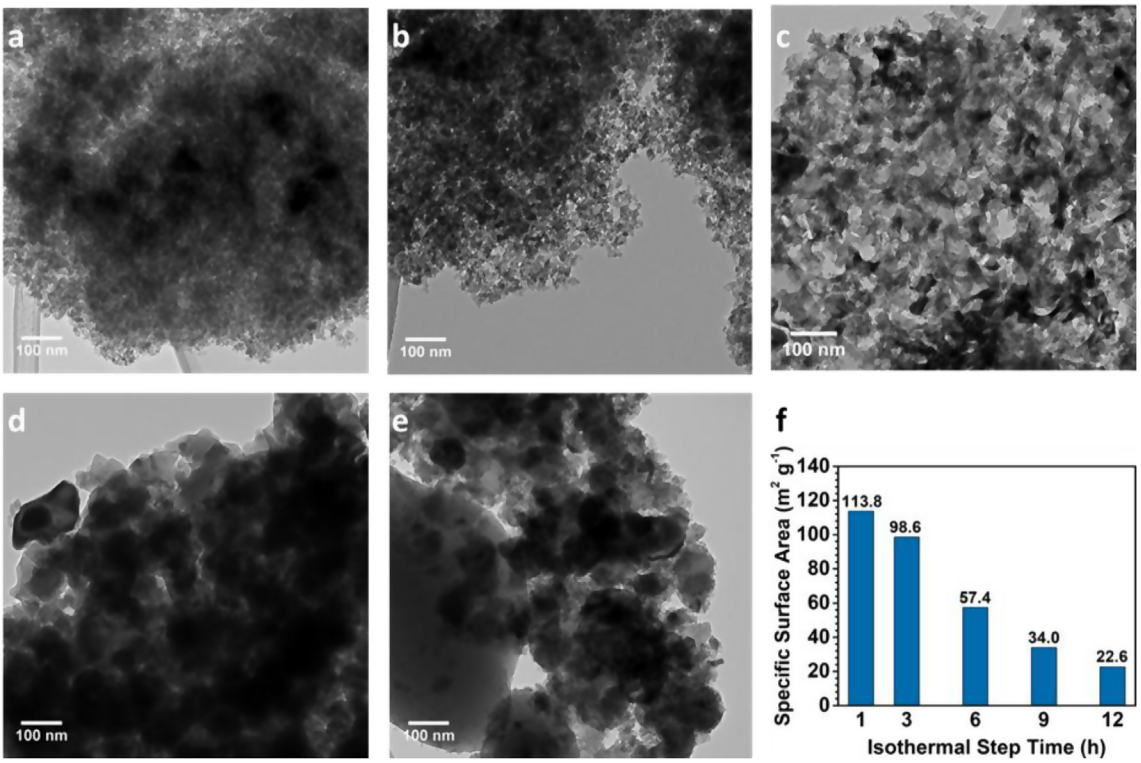

Fig. 4. TEM images of the Si materials from MRR at 580 °C with NaCl (Mg:NaCl = 1:1) for isothermal step time of (a) 1 h, (b) 3 h, (c) 6 h, (d) 9 h and (e) 12 h; (f) specific surface area of these Si from MRR at 580 °C.

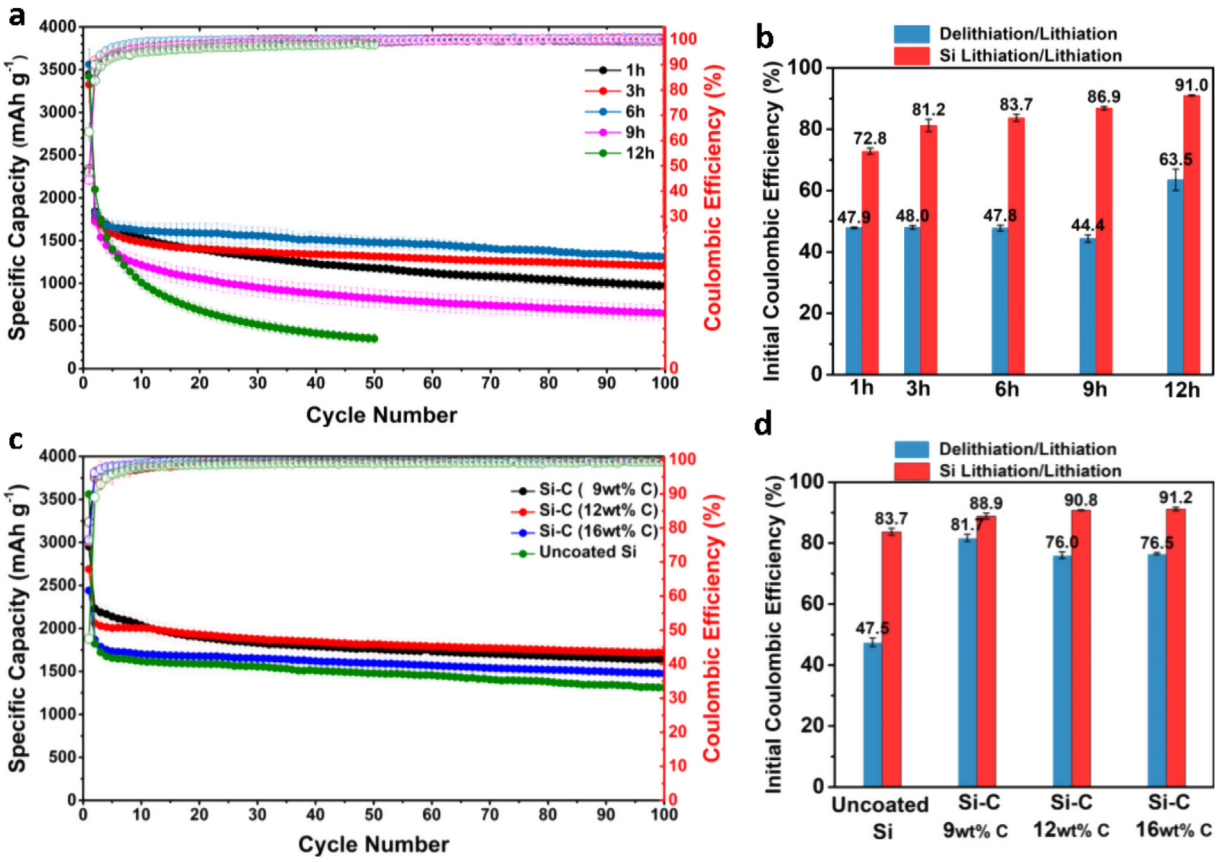

Fig. 5. (a) Cycle stability and (b) ICEs of the Si materials produced from MRR at 580 °C under different reaction duration; (c) Cycle stability and (d) ICEs of the Si from 6 h reaction duration after carbon coating via CVD. The lithiation-delithiation current is 100 mA g^{-1}.

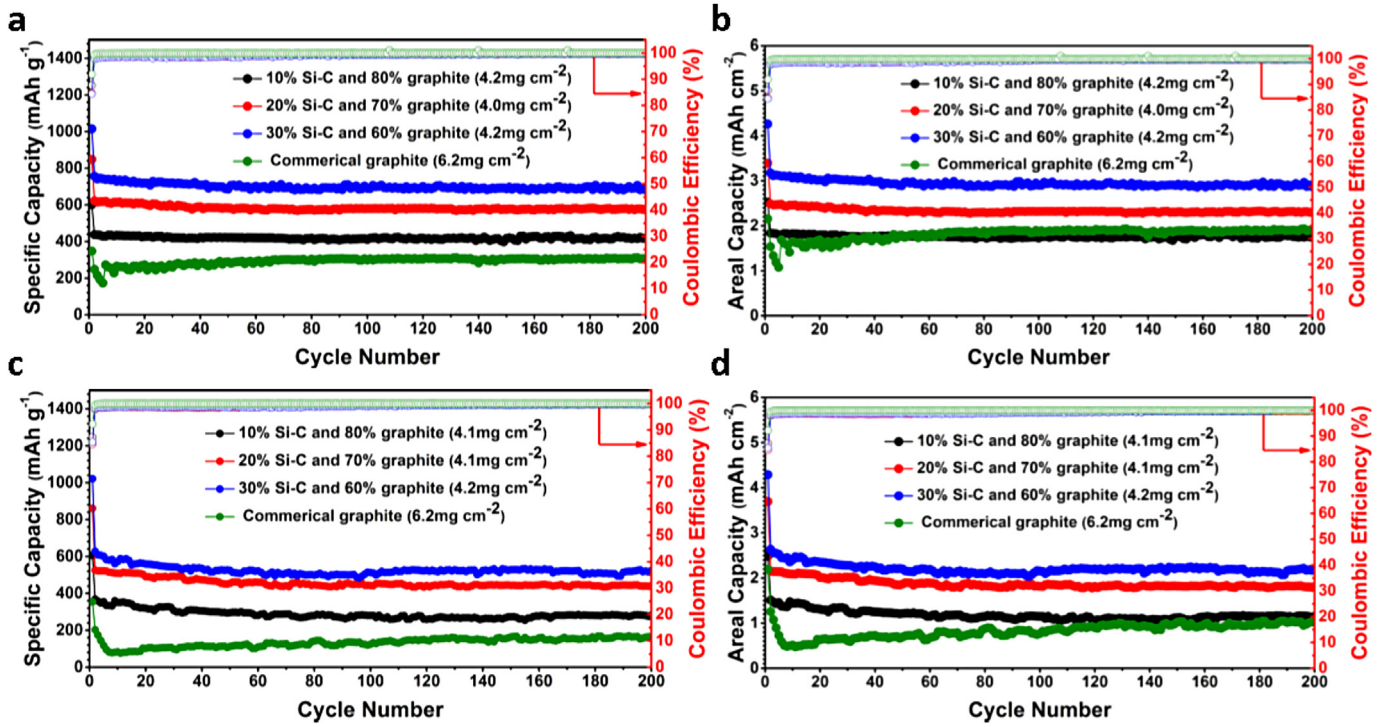

Fig. 6. Specific capacity, areal capacity, cycle stability, and CE of the electrodes containing 10 wt%, 20 wt% and 30 wt% Si-C composite in comparison with the pure graphite electrode at (a, b) 0.5 mA cm^{-2} and (c, d) 1 mA cm^{-2} lithiation-delithiation current. The first cycles are under 0.1 mA cm^{-2}.

Table 1
Performance of the electrode composed of Si-C composite and graphite in comparison with the pure graphite electrode.

Electrode	1st cycle Capacity (0.1 mA cm^{-2})	ICE	0.5 mA cm^{-2}				1.0 mA cm^{-2}			
			2nd Cycle Capacity	2nd Cycle CE	Capacity retention 200 cycles	Average CE	2nd Cycle Capacity	2nd Cycle CE	Capacity retention 200 cycles	Average CE
10 wt% Si-C	601 mAh g^{-1}	88%	437 mAh g^{-1}	98.3%	95%	99.5%	368 mAh g^{-1}	98.1%	76%	99.4%
20 wt% Si-C	848 mAh g^{-1}	85%	622 mAh g^{-1}	97.8%	92%	99.3%	526 mAh g^{-1}	97.9%	84%	99.2%
30 wt% Si-C	1014 mAh g^{-1}	84%	756 mAh g^{-1}	97.7%	90%	99.2%	626 mAh g^{-1}	98.1%	84%	99.2%
Graphite	348 mAh g^{-1}	92%	248 mAh g^{-1}	99.4%	–	99.9%	202 mAh g^{-1}	99.4%	81%	99.9%

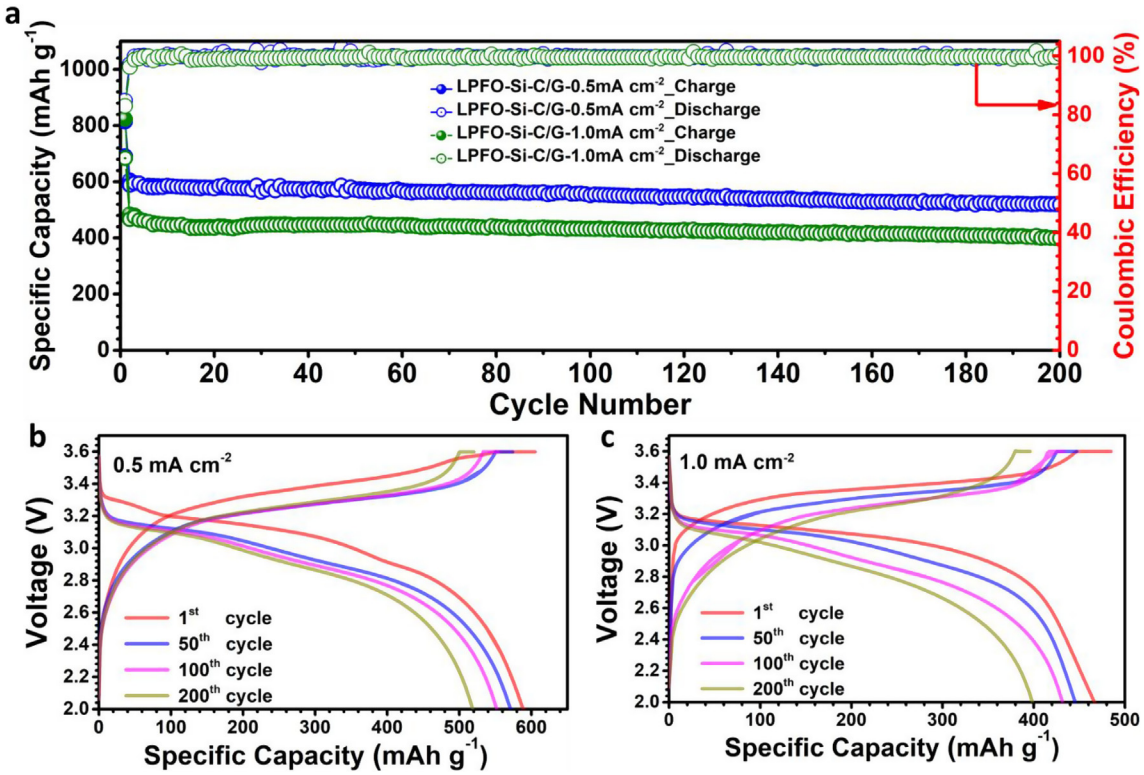

Fig. 7. (a) Cycle stability of the Si-C-graphite/$LiFePO_4$ full cells under current of 0.5 mA cm^{-2} and 1.0 mA cm^{-2}; Representative charge and discharge voltage profiles under current of (b) 0.5 mA cm^{-2} and (c) 1 mA cm^{-2}.

Information) were obtained via CVD using acetylene as the carbon source in a rotating tube furnace specifically designed for powder CVD process (MTI Corporation). The cycle stability and ICEs from these Si-C composites are shown in Fig. 5c and d, respectively, in comparison with the uncoated Si. From the specific capacity and cycle stability results in Fig. 5c, carbon coating via CVD at all weight ratio improves the overall capacity, which is attributed to the enhanced electronic conductivity, *i.e.*, charge transfer. The cycle stability is also improved by the carbon coating for all Si-C composites. The Si-C composite with 9 wt% carbon content shows the highest overall capacity, however, suffering from relatively fast capacity decay. On the other hand, the Si-C composite with 16 wt% carbon content showed superior cycle stability, but its overall capacity is only marginally higher than the bare Si. It is also clear that the ICEs calculated from both methods are significantly improved. For the conventional ICE, it is improved from 47.5% (uncoated Si) to 81.7% (9 wt% carbon), 76% (12 wt% carbon), and 76.5% (16 wt % carbon). The Si-C composite with 12 wt% carbon demonstrates the best overall performance by considering ICE, capacity and cycle stability. Therefore, this Si-C composite was selected to be further examined as a drop-in material to the graphite anode.

The most practical application of Si-C composite is to be used as the drop-in additive in the graphite anode to enhance the capacity. In our testing, the Si-C composite was mixed with graphite at three different weight ratios: 10 wt%, 20 wt% and 30 wt%. The corresponding graphite weight percentages are 80 wt%, 70 wt % and 60 wt%. The other 10 wt% of the electrode is composed of 4 wt% of CMC, 1 wt% of styrene-butadiene, and 5 wt% of acetylene black. The total areal loading of Si-C and graphite was typically 4.1 mg cm^{-2}. Fig. 6 shows the specific capacity (based on the total mass of Si-C and graphite), areal capacity, cycle stability and CE under current of 0.5 mA cm^{-2} (Fig. 6a and b) and 1.0 mA cm^{-2} (Fig. 6c and d). The first lithiation-delithiation cycle was carried under 0.1 mA cm^{-2} for activation: the initial capacities of the electrodes with 10 wt%, 20 wt% and 30 wt% of Si-C are 601 mAh g^{-1} (2.5 mAh cm^{-2}), 848 mAh g^{-1} (3.4 mAh cm^{-2}) and 1014 mAh g^{-1} (4.3 mAh cm^{-2}), respectively, superior to 348 mAh g^{-1} (2.2 mAh cm^{-2}) of the commercial graphite anode (areal loading 6.2 mg cm^{-2}). The ICEs under 0.1 mA cm^{-2} are 88% (10 wt% Si-C), 85% (20 wt% Si-C) and 84% (30 wt% Si-C), which are slightly lower than that of the graphite anode (92%). After the cycling current was increased to 0.5 mA cm^{-2} and 1.0 mA cm^{-2}, the electrodes containing Si-C composite still performed significantly better than the commercial graphite electrode as illustrated in Fig. 6 and summarized in Table 1. The representative lithiation-delithiation curves are shown in Figure S8 in Supporting Information.

The best all-around performance was demonstrated by the electrode containing 20 wt% Si-C and 70 wt% graphite: specific capacity and capacity retention are 622 mAh g^{-1} (areal capacity 2.5 mAh cm^{-2}) and 92% (200 cycles) at 0.5 mA cm^{-2}, and 526 mAh g^{-1} (areal capacity 2.1 mAh cm^{-2}) and 84% (200 cycles) at 1 mA cm^{-2}. To further demonstrate the relevant applications of the Si-C composite, we prepared the full cells (2032 coin cells) composed of the 20 wt% Si-C anode and commercial lithium iron phosphate ($LiFePO_4$) cathode with controlled amount of electrolyte at 14 μL per cell, approximately 5.6 g Ah^{-1}. The full cells were cycled with constant-current discharge followed by constant-current-constant-voltage (CCCV) charge with charge voltage at 3.6 V and cut off current at 0.05 mA cm^{-2}. Fig. 7a shows the cycle stability and CE of the full cell with specific capacity based on the total mass of Si-C and graphite [63]. Fig. 7b and c display the representative cycling curves under current of 0.5 mA cm^{-2} and 1.0 mA cm^{-2}, respectively. The initial capacities of the Si-C-graphite anode are 605 mAh g^{-1} (2.4 mAh cm^{-2}) under 0.5 mA cm^{-2} and 485 mAh g^{-1} (1.9 mAh cm^{-2}) under 1 mA cm^{-2}. Capacity retentions after 200 cycles are 88% at 0.5 mA cm^{-2} and 85% at 1 mA cm^{-2}.

4. Conclusions

In summary, we demonstrated an industrially feasible process to produce Si-C composites via magnesiothermic reduction of commercial silica and carbon coating via powder CVD. Through the kinetics study of the magnesiothermic reduction reaction, we obtained the key operational parameters to optimize the Si production. The produced Si-C composite materials demonstrated one of the best anode performances reported to date in open literature (Table S1 and Figure S9 in Supporting Information). We will continue to work on improving the initial Coulombic efficiency of the Si-C composite by refining the magnesiothermic reduction and carbon coating processes in our future investigations.

Acknowledgements

Z. Y. and J. G. are grateful to the financial support from Power Energy Solutions, Inc.

Appendix A. Supplementary data

Supplementary data to this article can be found online at https://doi.org/10.1016/j.nanoen.2019.06.041.

References

[1] R.K. Baldwin, K.A. Pettigrew, J.C. Garno, P.P. Power, G.-y. Liu, S.M. Kauzlarich, J. Am. Chem. Soc. 124 (2002) 1150–1151.
[2] J. Chen, H. Zhao, J. He, J. Wang, Rare Met. 30 (2011) 166–169.
[3] M. Nie, D.P. Abraham, Y. Chen, A. Bose, B.L. Lucht, J. Phys. Chem. C 117 (2013) 13403–13412.
[4] Z. Wen, G. Lu, S. Mao, H. Kim, S. Cui, K. Yu, X. Huang, P.T. Hurley, O. Mao, J. Chen, Electrochem. Commun. 29 (2013) 67–70.
[5] J.M. Tarascon, M. Armand, Nature 414 (2001) 359.
[6] X. Chen, K. Gerasopoulos, J. Guo, A. Brown, C. Wang, R. Ghodssi, J.N. Culver, ACS Nano 4 (2010) 5366–5372.
[7] X. Chen, K. Gerasopoulos, J. Guo, A. Brown, C. Wang, R. Ghodssi, J.N. Culver, Adv. Funct. Mater. 21 (2011) 380–387.
[8] H. Kim, B. Han, J. Choo, J. Cho, Angew Chem. Int. Ed. Engl. 47 (2008) 10151–10154.
[9] A.S. Arico, P. Bruce, B. Scrosati, J.-M. Tarascon, W. van Schalkwijk, Nat. Mater. 4 (2005) 366–377.
[10] J.B. Goodenough, K.-S. Park, J. Am. Chem. Soc. 135 (2013) 1167–1176.
[11] Y. Jin, S. Li, A. Kushima, X. Zheng, Y. Sun, J. Xie, J. Sun, W. Xue, G. Zhou, J. Wu, F. Shi, R. Zhang, Z. Zhu, K. So, Y. Cui, J. Li, Energy Environ. Sci. 10 (2017) 580–592.
[12] T. Shen, Z. Yao, X. Xia, X. Wang, C. Gu, J. Tu, Adv. Eng. Mater. (2018) 20.
[13] C. Martin, M. Alias, F. Christien, O. Crosnier, D. Bélanger, T. Brousse, Adv. Mater. 21 (2009) 4735–4741.
[14] X. Su, Q. Wu, J. Li, X. Xiao, A. Lott, W. Lu, B.W. Sheldon, J. Wu, Adv. Energy Mater. 4 (2014) 1300882.
[15] F. Dou, L. Shi, G. Chen, D. Zhang, Electrochem. Energy Rev. 2 (2019) 149–198.
[16] A. Magasinski, P. Dixon, B. Hertzberg, A. Kvit, J. Ayala, G. Yushin, Nat. Mater. 9 (2010) 353.
[17] M.A. Rahman, G. Song, A.I. Bhatt, Y.C. Wong, C. Wen, Adv. Funct. Mater. 26 (2016) 647–678.
[18] Q. Xu, J.-Y. Li, J.-K. Sun, Y.-X. Yin, L.-J. Wan, Y.-G. Guo, Adv. Energy Mater. 7 (2017) 1601481.
[19] X. Zuo, J. Zhu, P. Müller-Buschbaum, Y.-J. Cheng, Nano Energy 31 (2017) 113–143.
[20] A.L. Michan, M. Leskes, C.P. Grey, Chem. Mater. 28 (2015) 385–398.
[21] B. Philippe, R. Dedryvère, J. Allouche, F. Lindgren, M. Gorgoi, H. Rensmo, D. Gonbeau, K. Edström, Chem. Mater. 24 (2012) 1107–1115.
[22] S. Yang, X. Feng, S. Ivanovici, K. Mullen, Angew Chem. Int. Ed. Engl. 49 (2010) 8408–8411.
[23] Y. Wen, Y. Zhu, A. Langrock, A. Manivannan, S.H. Ehrman, C. Wang, Small 9 (2013) 2810–2816.
[24] R. Yi, F. Dai, M.L. Gordin, S. Chen, D. Wang, Adv. Energy Mater. 3 (2013) 295–300.
[25] C. Xu, F. Lindgren, B. Philippe, M. Gorgoi, F. Björefors, K. Edström, T. Gustafsson, Chem. Mater. 27 (2015) 2591–2599.
[26] Y. Sun, N. Liu, Y. Cui, Nat. Energy 1 (2016) 16071.
[27] M. Winter, J.O. Besenhard, M.E. Spahr, P. Novák, Adv. Mater. 10 (1998) 725–763.
[28] G.C. Hwang, D.A. Blom, T. Vogt, J. Lee, H.-J. Choi, S. Shao, Y. Ma, Y. Lee, Nat. Commun. 9 (2018) 5412.
[29] Z. Bao, M.R. Weatherspoon, S. Shian, Y. Cai, P.D. Graham, S.M. Allan, G. Ahmad, M.B. Dickerson, B.C. Church, Z. Kang, H.W. Abernathy 3rd, C.J. Summers, M. Liu, K.H. Sandhage, Nature 446 (2007) 172–175.
[30] Z. Favors, W. Wang, H.H. Bay, Z. Mutlu, K. Ahmed, C. Liu, M. Ozkan, C.S. Ozkan, Sci. Rep. 4 (2014) 5623.
[31] Y. Hwa, W.-S. Kim, B.-C. Yu, J.-H. Kim, S.-H. Hong, H.-J. Sohn, J. Power Sources 252 (2014) 144–149.
[32] P. Gao, H. Tang, A. Xing, Z. Bao, Electrochim. Acta 228 (2017) 545–552.
[33] A. Xing, J. Zhang, Z. Bao, Y. Mei, A.S. Gordin, K.H. Sandhage, Chem. Commun. (Camb) 49 (2013) 6743–6745.
[34] S. Choi, J.C. Lee, O. Park, M.-J. Chun, N.-S. Choi, S. Park, J. Mater. Chem. A 1 (2013) 10617.
[35] H. Zhong, H. Zhan, Y.-H. Zhou, J. Power Sources 262 (2014) 10–14.
[36] X. Ma, M. Liu, L. Gan, P.K. Tripathi, Y. Zhao, D. Zhu, Z. Xu, L. Chen, Phys. Chem. Chem. Phys. 16 (2014) 4135–4142.
[37] E.K. Richman, C.B. Kang, T. Brezesinski, S.H. Tolbert, Nano Lett. 8 (2008) 3075–3079.
[38] J. Ryu, D. Hong, M. Shin, S. Park, ACS Nano 10 (2016) 10589–10597.
[39] J. Xie, G. Wang, Y. Huo, S. Zhang, G. Cao, X. Zhao, Electrochim. Acta 135 (2014) 94–100.
[40] I. Barin, Edition, VCH, (1995).
[41] H. Yuan, R.S. Williams, Chem. Mater. 2 (1990) 695–700.
[42] C.R. Kao, Y.A. Chang, Acta Metall. Mater. 41 (1993) 3463–3472.
[43] I. Gutman, L. Klinger, I. Gotman, M. Shapiro, Solid State Ionics 180 (2009) 1350–1355.
[44] X. Liu, C. Giordano, M. Antonietti, J. Mater. Chem. 22 (2012) 5454.
[45] W. Luo, X. Wang, C. Meyers, N. Wannenmacher, W. Sirisaksoontorn, M.M. Lerner, X. Ji, Sci. Rep. 3 (2013) 2222.
[46] E.A. GIESS, J. Am. Ceram. Soc. 46 (1963) 374–376.
[47] A. Ginstling, B. Brounshtein, J. Appl. Chem. USSR 23 (1950) 1327–1338.
[48] J. Li, J.R. Dahn, J. Electrochem. Soc. 154 (2007) A156–A161.
[49] D. He, F. Bai, L. Li, L. Shen, H.H. Kung, N. Bao, Electrochim. Acta 169 (2015) 409–415.
[50] N. Liu, Z. Lu, J. Zhao, M.T. McDowell, H.W. Lee, W. Zhao, Y. Cui, Nat. Nanotechnol. 9 (2014) 187–192.
[51] X. Huang, X. Sui, H. Yang, R. Ren, Y. Wu, X. Guo, J. Chen, J. Mater. Chem. A 6 (2018) 2593–2599.
[52] J. Yang, Y.-X. Wang, S.-L. Chou, R. Zhang, Y. Xu, J. Fan, W.-x. Zhang, H. Kun Liu, D. Zhao, S. Xue Dou, Nano Energy 18 (2015) 133–142.
[53] H. Su, A.A. Barragan, L. Geng, D. Long, L. Ling, K.N. Bozhilov, L. Mangolini, J. Guo, Angew Chem. Int. Ed. Engl. 56 (2017) 10780–10785.
[54] S.H. Ng, J. Wang, D. Wexler, K. Konstantinov, Z.P. Guo, H.K. Liu, Angew Chem. Int. Ed. Engl. 45 (2006) 6896–6899.
[55] X. Shen, Z. Tian, R. Fan, L. Shao, D. Zhang, G. Cao, L. Kou, Y. Bai, J. Energy Chem. 27 (2018) 1067–1090.
[56] Q. Xu, J.-K. Sun, J.-Y. Li, Y.-X. Yin, Y.-G. Guo, Energy Storage Mater. 12 (2018) 54–60.
[57] B. Deng, L. Shen, Y. Liu, T. Yang, M. Zhang, R. Liu, Z. Huang, M. Fang, X. Wu, Chin. Chem. Lett. 28 (2017) 2281–2284.
[58] C. Natarajan, H. Fujimoto, K. Tokumitsu, A. Mabuchi, T. Kasuh, Carbon 39 (2001) 1409–1413.
[59] K.L. Choy, Prog. Mater. Sci. 48 (2003) 57–170.
[60] M. Yoshio, H. Wang, K. Fukuda, Angew. Chem. Int. Ed. 42 (2003) 4203–4206.
[61] K. Fu, L. Xue, O. Yildiz, S. Li, H. Lee, Y. Li, G. Xu, L. Zhou, P.D. Bradford, X. Zhang, Nano Energy 2 (2013) 976–986.
[62] R. Yi, F. Dai, M.L. Gordin, H. Sohn, D. Wang, Adv. Energy Mater. 3 (2013) 1507–1515.
[63] Y.S. Kim, G. Shoorideh, Y. Zhmayev, J. Lee, Z. Li, B. Patel, S. Chakrapani, J.H. Park, S. Lee, Y.L. Joo, Nano Energy 16 (2015) 446–457.